CHAPTER 5

INTRAMOLECULAR DYNAMICS ALONG ISOMERIZATION AND DISSOCIATION PATHWAYS

MARC JOYEUX

Laboratoire de Spectrométrie Physique (CNRS UMR 5588), Université Joseph Fourier, Grenoble 1, F-38402, St. Martin d'Hères Cedex, France

SERGY YU. GREBENSHCHIKOV, JENS BREDENBECK,[1] and REINHARD SCHINKE

Max-Planck-Institut für Strömungsforschung, D-37073 Göttingen, Germany

STAVROS C. FARANTOS

Institute of Electronic Structure and Laser Foundation for Research and Technology, Hellas, Greece; and Department of Chemistry, University of Crete, Iraklion 711 10, Crete, Greece

CONTENTS

[1]*Present Address*: Physikalisch-Chemisches Institut, Universität Zürich, CH-8057 Zürich, Switzerland.

Geometric Structures of Phase Space in Multidimensional Chaos: A Special Volume of Advances in Chemical Physics, Part A, Volume 130, edited by M. Toda, T Komatsuzaki, T. Konishi, R.S. Berry, and S.A. Rice. Series editor Stuart A. Rice.
ISBN 0-471-70527-6

I. INTRODUCTION

The purpose of this chapter is to review some properties of isomerizing (ABC $\leftrightarrow$ BCA) and dissociating (ABC $\rightarrow$ AB + C) prototype triatomic molecules, which are revealed by the analysis of their dynamics on precise ab initio potential energy surfaces (PESs). The systems investigated will be considered from all possible viewpoints—quantum, classical, and semiclassical mechanics—and several techniques will be applied to extract information from the PES, such as Canonical Perturbation Theory, adiabatic separation of motions, and Periodic Orbit Theory.

The key quantity in these studies is the strength of the coupling between reactive coordinates and perpendicular ones, where a coordinate is called reactive if it leads from reactants to products. The reactive coordinate is essentially an angle in the case of an isomerizing system and a stretching coordinate in the case of a dissociating system. The strength of the coupling between different degrees of freedom obviously depends on the choice of coordinates. When "natural" sets of coordinates, like valence or Jacobi ones, are used, it is rather rare that the couplings remain negligible up to the reaction threshold. In contrast, "optimized" sets of coordinates, which minimize the couplings between the various degrees of freedom up to and above the reaction threshold, can be derived rather straightforwardly for a certain number of isomerizing systems, like HCN $\leftrightarrow$ CNH or LiNC $\leftrightarrow$ NCLi. Section II describes in detail a procedure based on Canonical Perturbation Theory, which enables near-separation of motions for such isomerizing systems. Section II furthermore discusses vibrationally nonadiabatic tunneling in HCN $\leftrightarrow$ CNH, that is, the effect of remaining small couplings below the top of the adiabatic isomerization barrier on the shape of the wavefunctions along the perpendicular degrees of freedom.

For the nearly separable isomerizing systems studied in Section II, it is sufficient to increase the energy in the reactive degree of freedom to let the molecule explore the reaction pathway further and further and eventually react when the deposited energy is larger than the energy of the adiabatic reaction threshold. Recent studies dealing with the vibrational dynamics of small molecules (HCP, HOCl, HOBr...) have shown that this is certainly not the case for systems, which display a pronounced resonance between the reactive degree of freedom and a perpendicular one. Section III is devoted to the description of the subtle pattern of bifurcations, which the molecules mentioned above must

undergo in order to reach the reaction threshold, due to the existence of a 2:1 Fermi coupling between the reactive degree of freedom and perpendicular ones.

II. NEARLY SEPARABLE ISOMERIZING SYSTEMS

This section describes the dynamics of the isomerizing system HCN $\leftrightarrow$ CNH, for which near-separation of the various degrees of freedom can be achieved. It is first shown in Section II.A how Canonical Perturbation Theory (CPT) can be applied to this floppy molecule in order to find "optimized" sets of coordinates, which minimize the couplings between the various degrees of freedom. Section II.B further discusses the effects of the remaining small coupling terms on the tunneling between states with different quantum numbers in the perpendicular degrees of freedom.

A. Application of Canonical Perturbation Theory to Floppy Molecules

The basic idea of this section, which collects information scattered in Refs. 1–3, is to apply several unitary (or canonical) transformations to floppy systems initially described by ab initio or fitted potential energy surfaces and exact kinetic energy operators, in order to rewrite their Hamiltonian in terms of, as complete as possible, a set of good quantum numbers (or classical constants of the motion), plus some high-order small coupling terms that are eventually neglected at the end of the procedure. For HCN $\leftrightarrow$ CNH [1,2,4], LiNC $\leftrightarrow$ LiCN [5], and C_3 [6], a complete separation of motions was actually achieved after the high-order small coupling terms were neglected: As will be seen below, the final (or perturbative) Hamiltonian is formally a one-dimensional Hamiltonian in the bending angle, which is parameterized by the stretch quantum numbers.

The possibility of such a separation of motions is not obvious at all when looking at the PES of an isomerizing molecule. Figure 1 (left) shows as an example a two-dimensional cut in the (R, γ) plane of the three-dimensional PES for the HCN $\leftrightarrow$ CNH system obtained by Tennyson and co-workers [7,8]. R is the distance between H and the center of mass G of CN, while γ is the HGC angle ($\gamma = 0$ at the linear HCN configuration). For this figure, the third coordinate—that is, the distance r between C and N—is fixed to the HCN equilibrium value of 1.1528 Å. It is seen that the reaction pathway (or minimum energy path, MEP), which connects the HCN absolute minimum (at $\gamma = 0$) to the CNH relative one (at $\gamma = 180°$) through the saddle (at $\gamma \approx 80°$), displays a very strong curvature in the (R, γ) plane. Consequently, if the Hamiltonian matrix is built in the basis set constructed as the direct products of the one-dimensional functions for each Jacobi coordinate, then the couplings between the vectors of the basis are strong. The first step of the CPT procedure aimed at

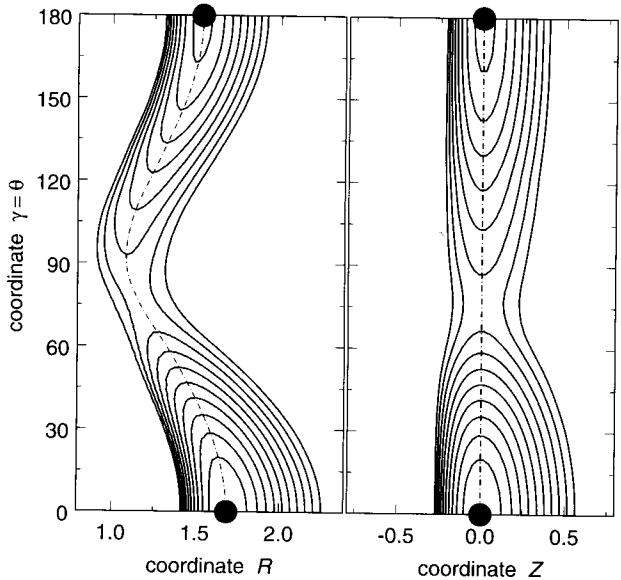

Figure 1. (**Left**) Two-dimensional cut in the (R, γ) plane of the three-dimensional PES for the HCN $\leftrightarrow$ CNH system obtained by Tennyson and co-workers [7,8]. R is the distance in Å between H and the center of mass, G, of CN, while γ is the HGC angle ($\gamma = 0$ at the linear HCN configuration, $\gamma = \pi$ at the linear CNH configuration). For this figure, the third coordinate (i.e., the distance r between C and N) is fixed to the HCN equilibrium value of 1.1528 Å. (**Right**) Same plot, but for coordinates (Z, θ) defined in Eq. (3).

minimizing these couplings consists in developing the initial Hamiltonian in Fourier series with respect to γ along the MEP and in Taylor series with respect to the stretch coordinates perpendicular to the MEP, in order to rewrite it in terms of simple operators.

More precisely, let us suppose that the initial Hamiltonian of the system is written in the form

$$\begin{aligned} H &= T + V(R, r, \gamma) \\ T &= \frac{1}{2\mu_r} p_r^2 + \frac{1}{2\mu_R} p_R^2 + \left(\frac{1}{2\mu_r r^2} + \frac{1}{2\mu_R R^2} \right) p_\gamma^2 \end{aligned} \tag{1}$$

where μ_r and μ_R stand for the reduced masses of C–N and H–CN, respectively, V is the PES expressed in terms of the Jacobi coordinates, and T is the classical expression of the kinetic energy of a triatomic molecule (we temporarily forget the additional term, which arises from the fact that the molecule is linear at equilibrium). Defining a grid γ_i $(i = 1, \ldots, i_{\max})$ of equally spaced points in γ,

such that $\gamma_1 = 0$ and $\gamma_{i_{\max}} = 180°$ ($i_{\max}$ is usually taken in the range 100–200), the MEP is first determined as the set of points $(R_{MEP}(\gamma_i), r_{MEP}(\gamma_i), \gamma_i)$, where $R_{MEP}(\gamma)$ and $r_{MEP}(\gamma)$ are solutions of

$$\left(\frac{\partial V}{\partial R}\right)_{R_{MEP}, r_{MEP}, \gamma} = \left(\frac{\partial V}{\partial r}\right)_{R_{MEP}, r_{MEP}, \gamma} = 0 \tag{2}$$

One also calculates by the method of finite differences the vectors $R'_{MEP}(\gamma_i)$ and $r'_{MEP}(\gamma_i)$ of the derivatives of R_{MEP} and r_{MEP} with respect to γ. For each value γ_i, the Hamiltonian is then rewritten in terms of the new set of conjugate variables

$$\begin{aligned} Z &= R - R_{MEP}(\gamma_i), \qquad p_Z = p_R \\ z &= r - r_{MEP}(\gamma_i), \qquad p_z = p_r \\ \theta &= \gamma, \qquad p_\theta = p_\gamma + R'_{MEP}(\gamma_i) p_R + r'_{MEP}(\gamma_i) p_r \end{aligned} \tag{3}$$

and expanded in Taylor series with respect to the coordinates Z and z. For each value of γ_i one thus obtains a series of the form

$$H(\theta = \gamma_i) = \sum_{\mathbf{m},\mathbf{n},N} h^{(i)}_{\mathbf{mn}N} Z^{m_1} z^{m_2} p_Z^{n_1} p_z^{n_2} p_\theta^N \tag{4}$$

where $\mathbf{m} = (m_1, m_2)$ and $\mathbf{n} = (n_1, n_2)$. By expanding each vector $h^{(i)}_{\mathbf{mn}N}$ ($i = 1, \ldots, i_{\max}$) in Fourier series with respect to $\theta = \gamma$ and rewriting $\cos(n\theta)$ in terms of $(\cos\theta)^n$, and likewise $\sin(n\theta)$ in terms of $(\sin\theta)(\cos\theta)^n$, the initial Hamiltonian H is cast in the form

$$H = \sum_{\mathbf{m},\mathbf{n},M,P,N} h_{\mathbf{mn}MPN} Z^{m_1} z^{m_2} (\cos\theta)^M p_Z^{n_1} p_z^{n_2} (\sin(\theta) p_\theta)^P p_\theta^{2N} \tag{5}$$

where $P = 0$ or $P = 1$. A two-dimensional cut in the (Z, θ) plane of the potential energy part of this expression is plotted in Fig. 1 (right) for $m_1 + m_2 \leq 12$ and $M \leq 24$. Wilson's GF formalism [9] is then applied to Eq. (5), in order to rewrite the Hamiltonian of the system in terms of the dimensionless normal coordinates (p_1, q_1) and (p_3, q_3) for the stretch degrees of freedom (for HCN $\leftrightarrow$ CNH, indexes 1 and 3 stand for the H–CN and C–N stretches, respectively).

At last, a few steps are necessary to make the expansion of Eq. (5) amenable to quantum CPT procedures: The dimensionless normal coordinates for the stretch degrees of freedom are expressed in terms of the ladder operators

$$a_k = \frac{1}{\sqrt{2}}(q_k + \mathrm{i}p_k), \qquad a_k^+ = \frac{1}{\sqrt{2}}(q_k - \mathrm{i}p_k) \tag{6}$$

where $i^2 = -1$ and $k = 1, 3$ (the convention $\hbar = 1$ is assumed throughout the manuscript), while p_θ^2 is replaced by the operator J^2, where

$$J^2 = -\frac{1}{\sin\theta}\frac{\partial}{\partial\theta}\sin\theta\frac{\partial}{\partial\theta} - \frac{1}{(\sin\theta)^2}\frac{\partial^2}{\partial\varphi^2} \tag{7}$$

and φ describes the rotation of the molecule around the axis with the smallest moment of inertia. One obtains

$$H = \sum_{\mathbf{m},\mathbf{n},M,P,N} H_{\mathbf{mn}MPN}(a_1^+)^{m_1}(a_1)^{n_1}(a_3^+)^{m_3}(a_3)^{n_3}(\cos\theta)^M\sigma^P(J^2)^N \tag{8}$$

where σ stands for the differential operator $\sin\theta\partial/\partial\theta$. Note that all of the operators that appear in Eq. (8) have simple matrix elements in the bases of the harmonic oscillator and of the spherical functions. Note also that symmetrization of Eq. (8), which is made necessary by the canonical transformations of Eq. (3), is postponed to an ulterior step (see below).

Following Van Vleck [10] Jordahl [11], and Kemble [12], the CPT procedure itself consists of a series of unitary transformations of increasing order s ($s = 1, 2, 3, \ldots$)

$$K = \exp(S)H\exp(-S) \tag{9}$$

where the initial operator H at order $s = 1$ is the expansion of Eq. (8) and the transformed Hamiltonian K obtained at order s serves as the initial operator H at order $s + 1$. The operator S, which appears in this equation, is anti-Hermitian. Reference to the current perturbation order s (in the form of subscripts or superscripts) will not be used, in order to avoid too complex notations. For the same reason, no artificial small parameter λ is introduced. The basic idea of CPT is to expand, at each order s, H, and K in the form

$$\begin{aligned} H &= \sum_{i=0}^{\infty} H^{(i)} \\ K &= \sum_{i=0}^{\infty} K^{(i)} \end{aligned} \tag{10}$$

where the $H^{(i)}$ and $K^{(i)}$ become smaller and smaller with increasing values of the order i. Actually, the ordering of the successive operators H (at $s > 1$) and K (at $s \geq 1$) is uniquely determined by the ordering of the initial operator H at order $s = 1$—that is, of Eq. (8). The choice of $H^{(0)}$ is particularly important, because the ability to solve the cohomology equation (see below) depends crucially on

this choice. Moreover, the number of terms to handle, and therefore the size of the required computer memory, depends on the ordering of the other $H^{(i)}$'s ($i > 0$). The best choice consists in retaining in $H^{(0)}$, at first order of the theory, only the sum of the harmonic oscillators for the stretch degrees of freedom, that is,

$$H^{(0)} = \sum_{i=1,3} \omega_i a_i^+ a_i \tag{11}$$

while the terms with $m_1 + m_3 + n_1 + n_3 + P + 2N = k$ are retained in $H^{(k)}$ if $M \neq 0$ and in $H^{(k-2)}$ if $M = 0$. An exception occurs for the pure bending terms in J^2 and $(\cos\theta)^M$, which are retained in $H^{(1)}$ rather than $H^{(0)}$, in order to satisfy Eq. (11). Each term $H^{(k)}$ is then symmetrized independently.

If one further assumes that, at order s of the perturbation procedure, the operator S is of the same order of magnitude as $H^{(s)}$ and $K^{(s)}$, then the relationship between the $K^{(i)}$ and the $H^{(i)}$ is simply obtained by expanding the exponential operators in Eq. (9) and equating the terms of the same order. One gets

$$\begin{aligned} &\text{If } i < s, \qquad K^{(i)} = H^{(i)} \\ &\text{If } i = s, \qquad K^{(s)} = H^{(s)} + [S, H^{(0)}] \\ &\text{If } i > s, \qquad K^{(i)} = H^{(i)} + \sum_m \frac{1}{n!} [\underbrace{S, \ldots [S}_{n \text{ times}}, H^{(m)}] \ldots] \end{aligned} \tag{12}$$

In the last equation, the summation runs over all integers m, for which there exists another integer n larger than or equal to 1, such that $m + ns = i$. The second equation of Eq. (12) is used to determine S by requiring that (at order s of the perturbation procedure) $K^{(s)}$ contains only the "physically important" terms of $H^{(s)}$. In other words, if R contains the terms of $H^{(s)}$, which are *not* wanted in $K^{(s)}$—that is, $R = H^{(s)} - K^{(s)}$—then S is determined by solving the so-called cohomology equation

$$[S, H^{(0)}] = -R \tag{13}$$

Straightforward calculations show that the choice of $H^{(0)}$ in Eq. (11) implies that an operator R of the form

$$R = \sum_{\mathbf{m},\mathbf{n},M,P,N} R_{\mathbf{mn}MPN} (a_1^+)^{m_1} (a_1)^{n_1} (a_3^+)^{m_3} (a_3)^{n_3} (\cos\theta)^M \sigma^P (J^2)^N \tag{14}$$

is canceled from $K^{(s)}$ if S is taken as

$$S = \sum_{\mathbf{m},\mathbf{n},M,P,N} \frac{R_{\mathbf{mn}MPN}}{\Delta_{\mathbf{mn}}} (a_1^+)^{m_1} (a_1)^{n_1} (a_3^+)^{m_3} (a_3)^{n_3} (\cos\theta)^M \sigma^P (J^2)^N \tag{15}$$

where $\Delta_{\mathbf{mn}} = (m_1 - n_1)\omega_1 + (m_3 - n_3)\omega_3$. The terms of K of order i higher than s are finally obtained from the third equation of Eq. (12) (note that the terms of order i smaller than s are not changed by the transformation at order s). Practically, the only tedious point in setting up a computer program consists in rewriting products of two terms $(a_1^+)^{m_1}(a_1)^{n_1}(a_3^+)^{m_3}(a_3)^{n_3}(\cos\theta)^M\sigma^P(J^2)^N$ as linear combinations of terms of the same form. This is achieved by using Sibert's formula [see Eq. (11) of Ref. 13) for stretch operators and the recurrence relations in Eq. (5) of Ref. 1 for bend operators.

The key of any CPT procedure is actually the choice, at each order s of the theory, of the terms of $H^{(s)}$ to be kept in $K^{(s)}$ and of those to be put in R, so that they are canceled by the unitary transformation at order s. The simplest perturbative Hamiltonian is obtained when only the terms, which are diagonal with respect to the stretch degrees of freedom, are kept in $K^{(s)}$, while all the other ones are assigned to R. In other words, all the terms of $H^{(s)}$ such that $\mathbf{m} \neq \mathbf{n}$ are canceled. When performing s unitary transformations with this criterion for the definition of R and then neglecting the terms $K^{(i)}$ such that $i > s$, one is left with a Hamiltonian of the form

$$K = \sum_{\mathbf{m},M,P,N} K_{\mathbf{m}MPN} (a_1^+)^{m_1} (a_1)^{m_1} (a_3^+)^{m_3} (a_3)^{m_3} (\cos\theta)^M \sigma^P (J^2)^N \tag{16}$$

which is called the "perturbative Hamiltonian of order s." The most useful expression for this Hamiltonian is obtained by expanding each product $(a_i^+)^{m_i}(a_i)^{m_i}$ in terms of the $(a_i^+ a_i)^{m_i} = v_i^{m_i}$, where the v_i are the stretch quantum numbers. One gets

$$K = \sum_{\mathbf{m},M,P,N} k_{\mathbf{m}MPN}\, v_1^{m_1}\, v_3^{m_3} (\cos\theta)^M \sigma^P (J^2)^N \tag{17}$$

where the $k_{\mathbf{m}MPN}$ are real coefficients. K is formally a one-dimensional Hamiltonian in the bending angle θ and its conjugate momentum. It depends only parametrically on the good quantum numbers for the stretch degrees of freedom.

Figure 2 shows the convergence of the CPT procedure described above, when it is applied to the ab initio surface for HCN $\leftrightarrow$ CNH computed by Tennyson and co-workers [7,8]. This figure indicates, for each order s of the perturbation procedure, the average arithmetic error between the energies of the lowest 101

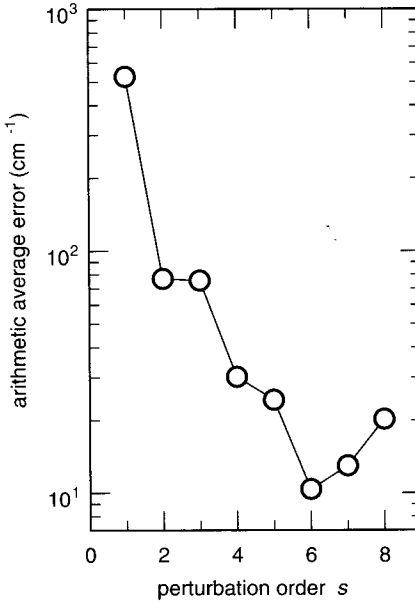

Figure 2. Plot, as a function of the order s of the perturbation procedure, of the average arithmetic error between the energies of HCN $\leftrightarrow$ CNH obtained for the ab initio surface of Refs. 7 and 8 and the perturbative Hamiltonian of Eq. (17). The lowest 101 rotationless states of the system are taken into account (see Tables VI and VII of Ref. 7). These states have up to 18 quanta of excitation in the bend degree of freedom and 12,400 cm^{-1} of vibrational energy above the quantum mechanical ground state.

rotationless states reported in Tables VI and VII of Ref. 7 and the corresponding energies computed with the perturbative Hamiltonian of order s [Eq. (17)]. The states taken into account have up to 18 quanta of excitation in the bend degree of freedom and 12,400 cm^{-1} of vibrational energy above the quantum mechanical ground state. Practically, the PES and the kinetic energy operator were initially Fourier expanded up to $(\cos\theta)^{M_{\max}}$ with $M_{\max} = 10$, because expansion to higher orders does not change significantly the results. Note, however, that all the trigonometric terms of higher order, which appear upon application of the CPT procedure, must be taken into account, so that the successive Hamiltonians remain Hermitian [if one orders the initial expansion of Eq. (8) as described in (and below) Eq. (11), then the trigonometric term with highest power one has to consider at order s of the perturbation procedure is $(\cos\theta)^{(s-2)M_{\max}}$]. It is well known that CPT leads to asymptotic series—that is, to series that converge for a certain number of iterations and then fluctuate or diverge. One therefore has to check somehow the convergence of the series of

perturbative Hamiltonians after each canonical transformation. It is seen in Fig. 2 that the best agreement with variational calculations is obtained for the sixth-order perturbative Hamiltonian, for which the average error is as low as about $10\,\mathrm{cm}^{-1}$.

Pseudo-potential energy curves are extracted from the perturbative Hamiltonian of Eq. (17) by retaining only the terms with $P = N = 0$—that is, the terms without differential operator. One obtains a one-dimensional pseudo-potential curve $V_{v_1,v_3}(\theta)$ for each pair of quantum numbers v_1 (H–CN stretch) and v_3 (C–N stretch)

$$V_{v_1,v_3}(\theta) = \sum_{\mathbf{m},M} k_{\mathbf{m}M00} v_1^{m_1} v_3^{m_3} (\cos\theta)^M \tag{18}$$

The lowest 11 pseudo-potential curves are drawn in Fig. 3. These curves can be used to determine, for example, if there is any chance to detect the system in the CNH well following its excitation to a given (v_1, v_2, v_3) state of HCN [14]—that is, if state (v_1, v_2, v_3) lies above or below the isomerization barrier for these values of v_1 and v_3. Figure 3 shows that, for HCN $\leftrightarrow$ CNH, an increase in the

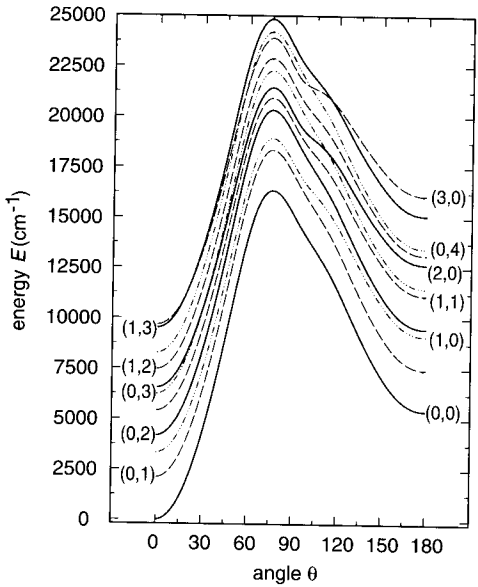

Figure 3. Plot of the lowest 11 pseudo-potential energy curves $V_{v_1,v_3}(\theta)$ obtained by applying sixth-order CPT to the HCN $\leftrightarrow$ CNH surface of Refs. 7 and 8. The stretch quantum numbers v_1 (H–CN stretch) and v_3(C–N stretch) are indicated for each curve as (v_1, v_3).

stretch quantum numbers essentially results in the shift of the energies of the HCN and CNH minima, as well as the isomerization threshold, by the corresponding linear combination of the fundamental frequencies. However, in other systems, like C_3 [6], variations of the stretch quantum numbers have a much more dramatic influence on the pseudo-potential energy curves. Moreover, the tunneling effect, which takes place slightly below the top of the isomerization barrier, is clearly seen when plotting, on the same graph, the wave functions of the states with given values of v_1 and v_3 and the corresponding pseudo-potential energy curve (see Fig. 4). We shall come back to this point in more detail in Section II.B.

Before concluding this section, let us just mention that, while all of the equations above refer explicitly to the Van Vleck quantum procedure [10–12,15], they are most straightforwardly adapted to the classical procedure based on Lie algebra [16–18] by replacing quantum commutators with Poisson brackets. Most of the concepts remain also valid for the classical

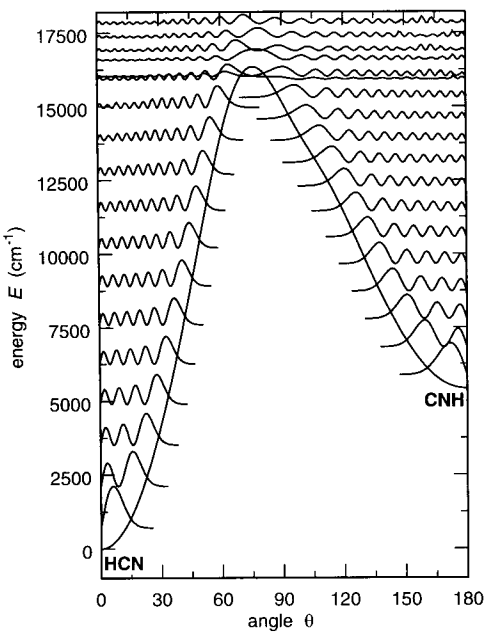

Figure 4. Plot of the pseudo-potential and the probability density for the pure bending states ($v_1 = v_3 = 0$) of the HCN ↔ CNH system versus bending angle θ. These results were obtained by applying sixth-order CPT to the ab initio surface of Tennyson and co-workers [7,8]. The vertical scale is the same for all probability plots, and the baseline for each plot coincides with the energy of the corresponding state.

Birkhoff–Gustavson procedure [19–21], although Eq. (12) has a slightly different form in this latter case [3].

B. Adiabatic Versus Nonadiabatic Delocalization in Isomerizing Systems

The theory described in Section II.A applies to the progressions of quantum mechanical "adiabatic" states. A state is adiabatic in the Ehrenfest sense, if the two perpendicular stretch quantum numbers v_1 and v_3 remain unchanged as the angle θ varies between 0° and 180°. As is known from the quantum mechanical calculations, all localized eigenstates of the non-rotating HCN and CNH molecules, trapped below the barrier on their respective adiabatic pseudo-potential curves (see Figs. 3 and 4), satisfy this definition. Moreover, many delocalized states located above their respective adiabatic barriers $V^+_{v_1,v_3}$ have the same assignment v_1 and v_3 on both HCN and CNH sides. Thus, the adiabatic approximation is realistic for a significant portion of the spectrum, including many of the delocalized states. The states belonging to the HCN and CNH well are usually assigned as $(v_1, v_2, v_3)_{\mathrm{HCN}}$ and $(v_1, v_2, v_3)_{\mathrm{CNH}}$, respectively. Alternatively, one might organize these states into adiabatic progressions $(v_1, v_2, v_3)_{\mathrm{ad}}$, by counting the bending quanta over the whole range of θ between 0° and 180°.

In view of the hitherto unsuccessful experimental search for eigenstates delocalized between the HCN and CNH isomers [14,22–28], the analysis of the mechanisms and spectral signatures of delocalization becomes central to theoretical studies. According to the adiabatic theory presented in Section II.A, states with excitation (v_1, v_3) in the perpendicular stretching coordinates are expected to remain localized even above the lowest adiabatic pseudo-potential barrier $V^+_{0,0}$. Indeed, in the adiabatic picture, these states become delocalized only if they are located close to or above the corresponding adiabatic potential barrier $V^+_{v_1,v_3}$, which can be located far above $V^+_{0,0}$ (see Fig. 3). This might explain the fact that no delocalized states were detected in the experiments that pumped energy in HCN through a combination of the bending and stretching modes [14,23,24]. Figure 5 illustrates more quantitatively the correlation between $V^+_{v_1,v_3}$ and the extent of delocalization. Each eigenstate can be ascribed probability densities in the HCN and CNH wells, P_{HCN} and P_{CNH}, respectively. Delocalization P_{del} of a normalized eigenstate is defined as the lesser of the two probabilities

$$P_{\mathrm{del}} = \min(P_{\mathrm{HCN}}, P_{\mathrm{CNH}}) \tag{19}$$

Figure 5 shows P_{del} for bending states in the pure and several combination progressions as a function of energy. The vertical solid line in each frame marks the position of the adiabatic barrier $V^+_{v_1,v_3}$. It is clear that full delocalization $P_{\mathrm{del}} = 50\%$ is reached only at and above the top of the adiabatic barrier,

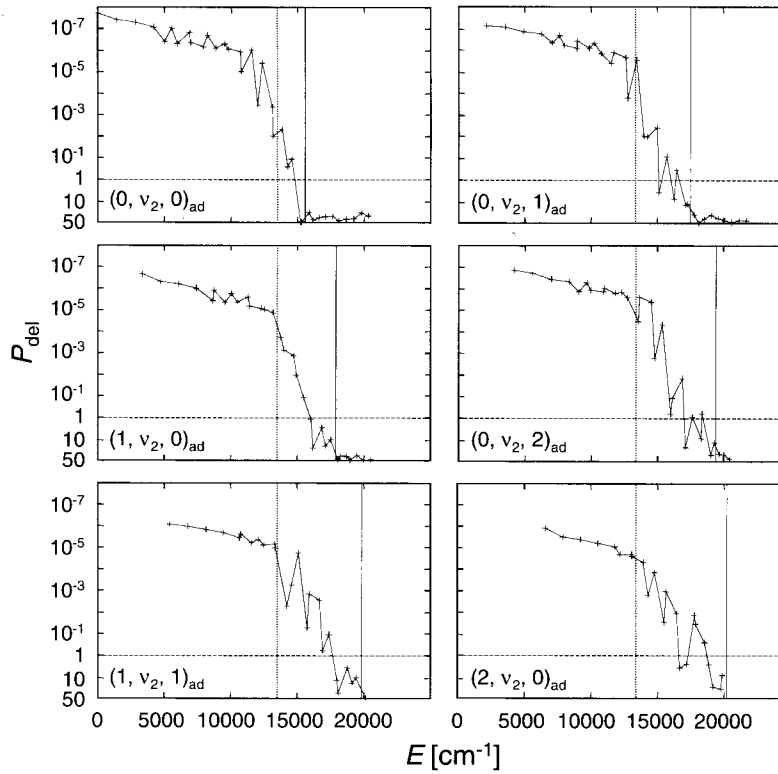

Figure 5. Plot of delocalization P_{del} (in %), defined in Eq. (19), as a function of the energy E above the ground vibrational state, for six bending progressions $(v_1, v_2, v_3)_{ad}$. The stretching quantum numbers v_1 and v_3 remain constant within each frame. The vertical solid lines indicate the position of the adiabatic barrier, $V^+_{v_1,v_3}$, for each progression. The energy of the PES' saddle point, close to $\gamma = 80°$, is marked with vertical dotted lines.

especially for low perpendicular excitations. Note that, due to couplings between the bending mode and the H–CN stretch, the height of the adiabatic barriers $V^+_{v_1,0}$ decreases with growing v_1. For example, the barrier $V^+_{6,0}$ (measured relative to the CNH minimum on the pseudo-potential curve) is only half as high as the barrier $V^+_{0,0}$. The higher the value of v_1, the lower the amount of bending excitation needed to achieve a certain degree of adiabatic delocalization.

At higher energies, it becomes increasingly difficult to organize delocalized eigenstates in adiabatic progressions. Quantum calculations show that, for many states, quantum numbers v_1 and/or v_3 are not conserved along θ. The stretching excitations instead change upon traversing the barrier separating HCN from CNH. Figure 6 illustrates this point. In the left-hand frame, the

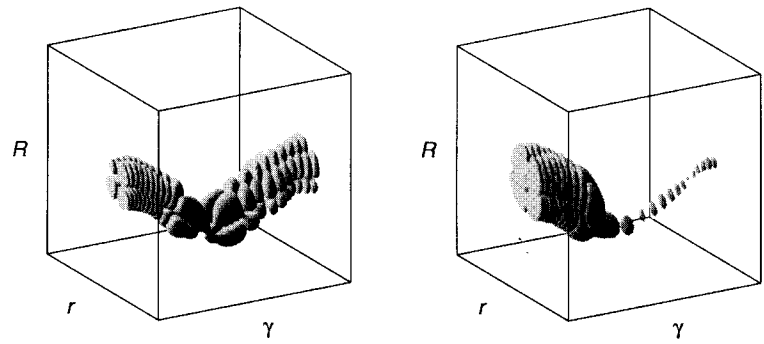

Figure 6. Wavefunctions of states 315 and 206 of the HCN $\leftrightarrow$ CNH system, with respective energies $E = 18,069\,\text{cm}^{-1}$ and $E = 15,750\,\text{cm}^{-1}$ above the quantum mechanical ground state. The figures show one particular contour $|\Psi(R,r,\gamma)|^2 = \text{const}$, where (R,r,γ) are the Jacobi coordinates. (**Left**) The adiabatically delocalized state 315, which is assigned as $(1,40,1)_{\text{ad}}$. (**Right**) The nonadiabatically delocalized state 206, which can be assigned as $(1,16,1)_{\text{HCN}}$ but displays the nodal structure of $(0,24,0)_{\text{CNH}}$ on the CNH side.

three-dimensional (3D) wavefunction of an adiabatically delocalized state is shown. It has one quantum of excitation in each perpendicular mode all the way from HCN to CNH. The theory of Section II.A can be applied to it. In the right-hand frame, another delocalized state is shown. On the HCN side, it has the same nodal pattern as the adiabatically delocalized state shown in the left-hand frame of Fig. 6. On the CNH side, the state has instead no node in the stretching coordinates. This is an example of a "nonadiabatically" delocalized eigenstate. Note that nonadiabatic delocalization is due to small terms belonging to one of the $K^{(i)}$ $(i > s)$ which, in Section II.A, were neglected after the desired number s of transformations was performed. These small terms therefore do not appear in the expression of the effective Hamiltonian of Eq. (17), so that this Hamiltonian cannot reproduce the nonadiabatic delocalization effect.

In the remainder of this section, we consider the properties of the nonadiabatically delocalized states of HCN $\leftrightarrow$ CNH in more detail. We argue that this type of delocalization becomes dominant and responsible for HCN $\leftrightarrow$ CNH isomerization above the top of the potential barrier. Our analysis is based on numerically exact quantum mechanical calculations for the HCN $\leftrightarrow$ CNH system performed using the PES of Bowman et al. [29], which reproduces the experimental vibration and vibration–rotation eigenenergies to within $60\,\text{cm}^{-1}$ or better even at high energies. For the present study, we calculated the energies of the first 600 states of the nonrotating molecule—that is, up to about $22{,}200\,\text{cm}^{-1}$ above the vibrational ground state—using successive truncation-diagonalization [30,31]. The eigenstates are converged

to within 0.5 cm^{-1} or better. The first 455 eigenstates and some of the states at higher energies were assigned using visual inspection of their wavefunctions, in order to provide an as complete as possible characterization of the localized and delocalized states.

The correlation between the height of the adiabatic barrier and the onset of delocalization is clearest in the pure bending progression $(0, v_2, 0)$ shown in Fig. 5. Delocalization patterns in other progressions are more involved. An example is provided by the progression $(1, v_2, 0)$, for which full delocalization, $P_{\text{del}} = 50\%$, is achieved only at $E \geq V^+_{1,0}$. However, several states below this barrier are also delocalized to some extent, with P_{del} ranging from 1% to 10%. A closer look indicates that the first weakly delocalized states ($P_{\text{del}} = 1.2\%$) appears near the top of the barrier of the lowest adiabatic curve $V^+_{0,0}$. In other words, weakly delocalized states in the progression $(1, v_2, 0)$ appear in the vicinity of the fully delocalized states of the progression $(0, v_2, 0)$. A similar behavior is found for other progressions shown in Fig. 5. Visual inspection of the three-dimensional eigenfunctions shows that the majority of the states with $P_{\text{del}} \leq 10\%$ are nonadiabatically delocalized. For these nonadiabatically delocalized states, $v_1(\text{HCN}) \neq v_1(\text{CNH})$ and/or $v_3(\text{HCN}) \neq v_3(\text{CNH})$. Their assignment to pure progressions is based on the nodal structure of the strongest component of the wavefunction.

Visual inspection of the wavefunctions reveals another feature of the nonadiabatically delocalized states, which is crucial for rationalizing the effect and building up a model. Namely, the perpendicular quantum numbers v_1 and v_3 of the weak component of these states systematically coincide with the perpendicular quantum numbers of an adjacent adiabatically delocalized state. This suggests that weak delocalization is induced by coupling between a certain zero-order localized state $|\phi_k\rangle$ and a neighboring adiabatically delocalized state $|\chi_v\rangle$. Suppose that both $|\phi_k\rangle$ and $|\chi_v\rangle$ are known. Then, a nonadiabatically delocalized state $|\Psi_k\rangle$ can be expressed as

$$|\Psi_k\rangle \approx \alpha_k|\phi_k\rangle + \beta_k|\chi_v\rangle \tag{20}$$

where $|\phi_k\rangle$ is assumed to be completely localized in one of the potential wells, while $|\chi_v\rangle$ is delocalized between the HCN and CNH isomers. By construction, one has $P_{\text{del}} = |\beta_k|^2 P_{\text{del}}(\chi_v)$, where $P_{\text{del}}(\chi_v)$ is the probability density of $|\chi_v\rangle$ in the potential well where $|\phi_k\rangle \equiv 0$. The wavefunctions $|\phi_k\rangle$ and $|\chi_v\rangle$ are normalized, but they are in general not orthogonal. Their overlap $S_{kv} = \langle\phi_k|\chi_v\rangle$ controls the coefficients α_k and β_k and, hence, the extent of delocalization P_{del}:

$$\begin{aligned} \alpha_k &= (1 - S_{kv}^2)^{-1/2} \\ \beta_k &= -\alpha_k S_{kv} \\ P_{\text{del}} &= P_{\text{del}}(\chi_v) S_{kv}^2/(1 - S_{kv}^2) \end{aligned} \tag{21}$$

If the zero-order basis is properly chosen, the model of Eq. (20) is a sensitive indicator of those couplings in the molecule that lead to delocalization. This in turn can be used to describe the delocalization mechanisms in HCN $\leftrightarrow$ CNH.

The states $|\phi_k\rangle$ and $|\chi_v\rangle$ in Eq. (20) can be chosen in a variety of ways. For example, the delocalized states calculated in Section II.A using the one-dimensional pseudo-potential curves can in principle be used as functions $|\chi_v\rangle$. The states $|\phi_k\rangle$ localized in each potential well can also be determined using the same pseudo-potential curves (eventual tunneling contributions should be neglected). Unfortunately, the accuracy of the adiabatic pseudo-potentials of Section II.A, although sufficient for predicting the positions of the energy levels to within a few tens of reciprocal centimeters (compared to the variationally calculated energies), is not high enough to describe the subtle effects of weak delocalization. For this reason, it is more appropriate to construct the basis states using three-dimensional quantum mechanical calculations. We define the localized basis states $|\phi_k\rangle$ as solutions of the "restricted" Schrödinger equation in the isolated wells. The dividing surface between the HCN and CNH parts of the PES is determined in molecular coordinates. The potential energy along the dividing surface in the restricted calculations is set to some large number which guarantees that wavefunctions are localized in one of the potential wells. Thus, solutions in one well are independent of the solutions in the other and can be used as $|\phi_k\rangle$. Next, this basis is augmented by the adiabatically delocalized eigenstates $|\chi_v\rangle$ of the original unrestricted Schrödinger equation: This is in accord with our conjecture that adiabatically delocalized states are the main perturbers causing weak delocalization.

The wavefunctions $|\phi_k\rangle$ and $|\chi_v\rangle$ solve different Schrödinger equations and therefore are not orthogonal. Since the overlap integrals between them are the measure of nonadiabatic delocalization, one first calculates S_{kv} between all localized and delocalized states. This identifies the most important couplings in the system, as well as the states that can be nonadiabatically delocalized. Next, the weakly delocalized eigenstates are reconstructed using Eq. (20) and compared to the exact results. Note that this procedure is somewhat reminiscent of the well-known tier model widely used in the investigations of intramolecular energy redistribution [32]. State $(2, 16, 0)_{\mathrm{HCN}}$ provides a typical example (see Fig. 7). Its nonadiabatic delocalization is entirely due to the coupling with the adiabatically delocalized state $(0, 56, 0)_{\mathrm{ad}}$, which lies only $11\,\mathrm{cm}^{-1}$ below $(2, 16, 0)_{\mathrm{HCN}}$. This is confirmed by reconstructing the weakly delocalized state using Eq. (20) and comparing the obtained nodal structure with the exact one. The extent of delocalization of the reconstructed wavefunction, $P_{\mathrm{del}} = 3.4\%$, is in excellent agreement with the exact result, $P_{\mathrm{del}} = 3.6\%$. The eigenenergy and the rotational constant of this state are also accurately reproduced within the simple approximation of Eq. (20).

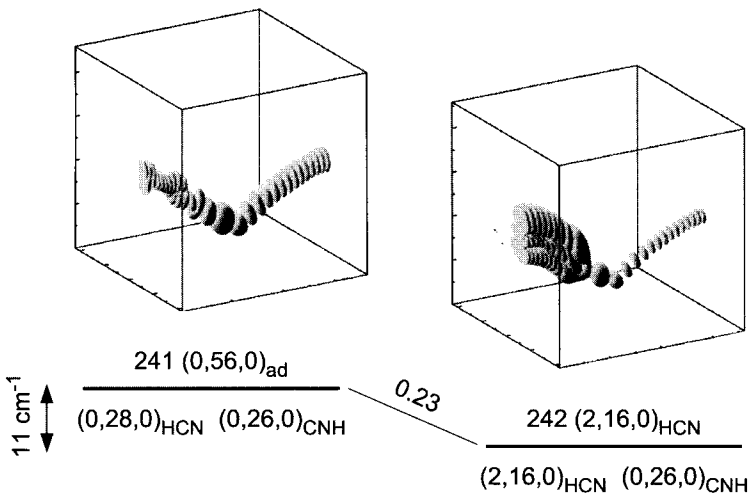

Figure 7. Simple two-state coupling scheme in HCN ↔ CNH, according to Eq. (20). (**Left**) Wavefunction of the adiabatically delocalized state 241 ($E = 16,612\,\mathrm{cm}^{-1}$), which is assigned as $(0,56,0)_{\mathrm{ad}}$. This is state $|\chi_v\rangle$ of Eq. (20). (**Right**) Wavefunction of the resulting nonadiabatically delocalized state 242 ($E = 16,623\,\mathrm{cm}^{-1}$), which can be assigned as $(2,16,0)_{\mathrm{HCN}}$ but displays the nodal structure of $(0,26,0)_{\mathrm{CNH}}$ on the CNH side. This is state $|\Psi_k\rangle$ of Eq. (20). The various assignments refer to the adiabatic description (upper) and to the nodal structures in the isolated wells (lower). The value of the overlap integral S_{kv} is indicated along the line connecting the two states. The wavefunctions are shown in the same representation as in Fig. 6.

Some of the localized basis functions couple to more than one adiabatically delocalized states. In this case, the model of Eq. (20) should be generalized to accommodate these couplings:

$$|\Psi_k\rangle \approx \alpha_k|\phi_k\rangle + \sum_{v=1}^{N_k} \beta_{kv}|\chi_v\rangle \tag{22}$$

where the coefficients α_k and β_{kv}, and the delocalization P_{del}, are given by

$$\begin{aligned} \alpha_k &= \left(1 - \sum_{v=1}^{N_k} S_{kv}^2\right)^{-1/2} \\ \beta_{kv} &= -\alpha_k S_{kv} \\ P_{\mathrm{del}} &= \sum_{v=1}^{N_k} |\beta_{kv}|^2 P_{\mathrm{del}}(\chi_v) \end{aligned} \tag{23}$$

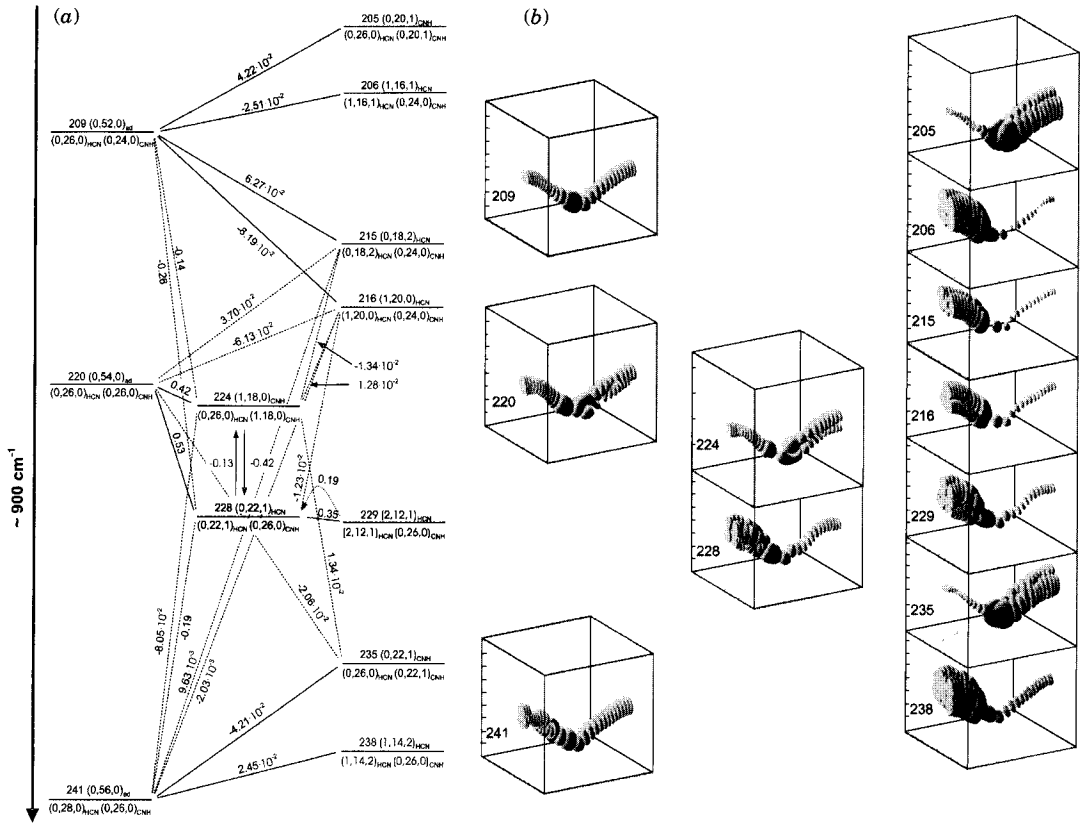

Figure 8. The scheme of interstate couplings leading to nonadiabatic delocalization in HCN ↔ CNH, in an energy window of 900 cm^{-1} centered around 16,200 cm^{-1} above the quantum mechanical ground state. (**a**) The structure of the energy levels, their assignments (upper, adiabatic; lower, according to the nodal structure in the isolated wells), and overlap integrals S_{kv} (numbers on the lines connecting pairs of states). The extent of delocalization diminishes from left to right. (**b**) Wavefunctions of the energy levels shown in (*a*). The wavefunctions are shown in the same representation as in Fig. 6.

This model can be used to uncover the complicated network of interstate couplings leading to nonadiabatic delocalization. An example of such a coupling scheme is presented in Fig. 8a. These states lie approximately 16,000 cm^{-1} above the ground vibrational state. The energy interval of about 900 cm^{-1} comprises 37 states, of which only three are adiabatically delocalized. They belong to the progression $(0, v_2, 0)$ and are collected in the left column of Fig. 8a. The adiabatically delocalized states lie above the respective barrier $V^+_{0,0}$. All other states belong to progressions, which are adiabatically trapped below the respective adiabatic barriers $V^+_{v_1,v_3}$. Nevertheless, all the trapped states are nonadiabatically delocalized. This is clearly seen in Fig. 8b, which shows some of the corresponding wavefunctions. Nonadiabatic delocalization of two states, 224 and 228, is particularly strong, with respective values $P_{del} = 20.0\%$ (224) and $P_{del} = 6.9\%$ (228). These states are shown in the middle column of the diagram in Fig. 8a. The states in the right column are more weakly delocalized ($P_{del} = 1.1\%$). Strong and weak couplings between eigenstates are indicated by the solid and dotted lines, respectively. The numbers above the lines are the values of the overlap integrals S_{kv} for the pair of states in question. This scheme can be considered as a pictorial guide to the choice of the coupling model for a particular state. For example, states 205 and 206 are perturbed only by the adiabatically delocalized state $(0, 52, 0)_{ad}$ in the left column. For them, Eq. (20) is appropriate. For most other states in the right and middle columns, the multiple perturber model of Eq. (22) appears to be more adequate.

Figure 8 demonstrates how the delocalization, initially carried by three adiabatically delocalized states, spreads over the adjacent eigenfunctions. Note that one can distinguish between direct and indirect interactions of eigenstates. Delocalization of states 205 and 206 is a result of the direct coupling with the adiabatically delocalized state 209. More complicated is the example of state 229 (right column in Fig. 8). In the zeroth-order approximation, this state is assigned as $(2, 12, 1)_{HCN}$. Its (weak) nodal structure in the CNH well coincides with that of the adiabatically delocalized state 220 (left column), although the direct overlap between these two states is vanishingly small. In fact, the nodal structure of state 229 in the CNH well is due to its coupling to the neighboring state 228 (middle column), which, in turn, is strongly coupled to the adiabatic state 220. The coupling scheme in Fig. 8 contains even more complicated coupling chains, which develop between the localized and delocalized states, thus leading to spreading of the weak delocalization over the entire spectrum. Adiabatically delocalized eigenfunctions play the role of critical nuclei necessary to initiate this process. The avalanche-like expansion of weak delocalization, initiated by the adiabatically delocalized states, is the main reason for the increase in the density of states with $P_{del} \geq 1\%$ with growing energy. This is illustrated in Fig. 9, where the total density of states is compared with the density of delocalized states.

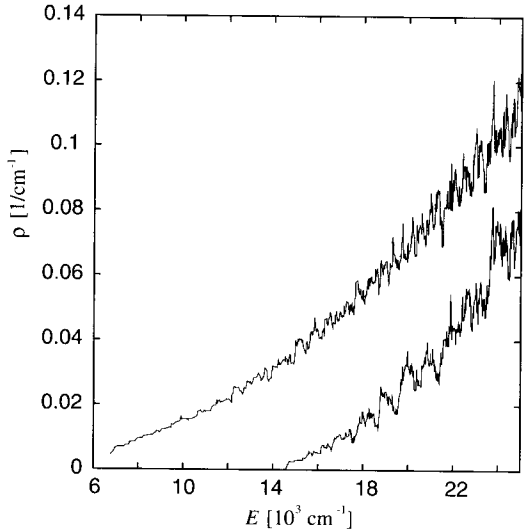

Figure 9. The density of states in the HCN ↔ CNH system as a function of energy above the ground vibrational state. The upper curve shows the full density of states. The lower curve corresponds to the density of delocalized states with $P_{\text{del}} > 1\%$.

III. RESONANTLY COUPLED ISOMERIZING AND DISSOCIATING SYSTEMS

Section II dealt with the system HCN ↔ CNH, for which the various degrees of freedom can be nearly separated. Section III is instead devoted to the description of the dynamics of the isomerizing and dissociating systems HCP ↔ CPH, HOCl → HO + Cl and HOBr → HO + Br, for which there exists a strong coupling (namely, a 1:2 Fermi resonance) between the reactive degree of freedom and a perpendicular one. A feature that is common to isomerization and dissociation reactions is the large anharmonicity along the reaction pathway. Based on the analysis of two integrable models—the Dunham expansion and the Fermi resonance Hamiltonian—Section III.A describes how the folding of the polyads (i.e., the closely spaced groups of states coupled by the Fermi resonance) caused by these large anharmonicities combines with the Fermi nonlinear coupling to produce a saddle-node bifurcation, where quantum states, which stretch along the reaction pathway, are created. These saddle-node bifurcations are, however, just the first step of the subtle pattern of bifurcations, which these systems must undergo in order to reach the reaction threshold. Relying mostly on the classical analysis of the ab initio PESs, Section III.B describes this pattern in

more detail, particularly emphasizing the correspondence between the quantum mechanical and classical descriptions.

A. Polyad Folding and Saddle-Node Bifurcations

It has been shown recently that the vibrational spectra of HCP [33–36], HOCl [36–39], and HOBr [40,41] obtained from quantum mechanical calculations on global ab initio surfaces can be reproduced accurately in the low to intermediate energy regime (75% of the isomerization threshold for HCP, 95% of the dissociation threshold for HOCl and HOBr) with an integrable Fermi resonance Hamiltonian. Based on the analysis of this Hamiltonian, this section proposes an interpretation of the most salient feature of the dynamics of these molecules, namely the first saddle-node bifurcation, which takes place in the intermediate energy regime.

The Fermi resonance Hamiltonian consists of two terms. The first one, H_D, is the Dunham expansion, which characterizes the uncoupled system, while the second term, H_F, is the Fermi resonance coupling, which describes the energy flow between the reactive mode and one perpendicular mode. For the three systems, HCP $\leftrightarrow$ CPH, HOCl $\rightarrow$ HO + Cl and HOBr $\rightarrow$ HO + Br, the reactive degree of freedom is the slow component of the Fermi pair and will therefore be labeled s, while the fast component will be labeled f. Thus, the resonance condition writes $\omega_f \approx 2\omega_s$. More explicitly, for HCP the slow reactive mode is the bend (mode 2) and the fast one is the CP stretch (mode 3), while for HOCl and HOBr the slow mode is the OX stretch (X = Cl,Br) (mode 3) and the fast one is the bend (mode 2). The third, uncoupled mode—that is, the CH stretch (mode 1) for HCP and the OH stretch (mode 1) for HOCl and HOBr—will be labeled u. With these notations, the Dunham expansion writes in the form

$$H_D = \sum_{i=s,f,u} \omega_i I_i + \sum_{i,k} x_{ik} I_i I_k + \sum_{i,k,m} y_{ikm} I_i I_k I_m + \cdots \tag{24}$$

where

$$I_i = \frac{1}{2}(p_i^2 + q_i^2) = a_i^+ a_i + \frac{d_i}{2} = v_i + \frac{d_i}{2} \tag{25}$$

In Eq. (25), (p_i, q_i) is the set of conjugate dimensionless normal coordinates for mode i, a_i^+ and a_i are the corresponding creation and annihilation operators, v_i is the quantum number for this degree of freedom, and d_i is its degeneracy (d_i is equal to 2 for the bend in HCP and equal to 1 for all other degrees of freedom considered here). I_i is the classical action integral for mode i and Eq. (25) just

expresses the Einstein–Brillouin–Keller (EBK) quantization rule [42–45] for this mode. Quantum mechanically, the Fermi resonance term is written as

$$H_F = (a_s a_s a_f^+ + a_s^+ a_s^+ a_f)\left(k_0 + \sum_{i=s,f,u} k_i I_i + \cdots\right) \tag{26}$$

while its classical expression involves the angles $\varphi_i = -\tan^{-1}(p_i/q_i)$ conjugate to the I_i's, that is,

$$H_F = 2\cos(\varphi_f - 2\varphi_s) I_s \sqrt{I_f}\left(k_0 + \sum_{i=s,f,u} k_i I_i + \cdots\right) \tag{27}$$

See Table I of Ref. 34, Table II of Ref. 39 and Table I of Ref. 41 for numerical values of the coefficients ω_i, x_{ik}, y_{ikm}, $k_i, \ldots$. Note that there are two misprints in Table II of Ref. 39: One should read $y_{233} = +0.2503\,\mathrm{cm}^{-1}$ and $y_{123} = -0.4304\,\mathrm{cm}^{-1}$.

Let us first neglect the Fermi resonance and analyze the dynamics of the uncoupled systems described by the Dunham expansion alone [Eq. (24)]. Because of the resonance condition $\omega_f \approx 2\omega_s$, quantum states are organized in clumps, or "polyads." Each polyad is defined by two quantum numbers, namely the number v_u of quanta in the uncoupled degree of freedom and the so-called polyad number P:

$$P = 2v_f + v_s \tag{28}$$

A polyad with quantum numbers v_u and P is labeled $[v_u, P]$. Polyads are separated by large energy gaps at low energies but overlap more and more widely as energy increases. It turns out that for the three molecules HCP, HOCl, and HOBr, the difference $2\omega_s - \omega_f$ is small (resonance condition) *and* positive. Therefore, at low P values, polyad $[v_u, P]$ organizes as follows. The state with lowest energy has quantum numbers $(v_s, v_f) = (0, P/2)$ (if P is even) or $(v_s, v_f) = (1, (P-1)/2)$ (if P is odd). The state with highest energy has quantum numbers $(v_s, v_f) = (P, 0)$. In between, the energies of the $\mathrm{int}(P/2) + 1$ states of the polyad increase monotonously with the number of quanta v_s in the reactive degree of freedom. Because of the large (negative) anharmonicity along the reaction pathway, this description does not hold for large values of P. Indeed, if P (and therefore v_s) becomes sufficiently large, then the *linear* harmonic energy gap $2\omega_s - \omega_f$ between two successive states of the polyad can become smaller than the *quadratic* (or higher-order) anharmonic corrections. For these higher values of P, the energies of the $\mathrm{int}(P/2) + 1$ states of the polyad are an increasing function of v_s up to a certain value of v_s, and then a *decreasing* function of v_s.

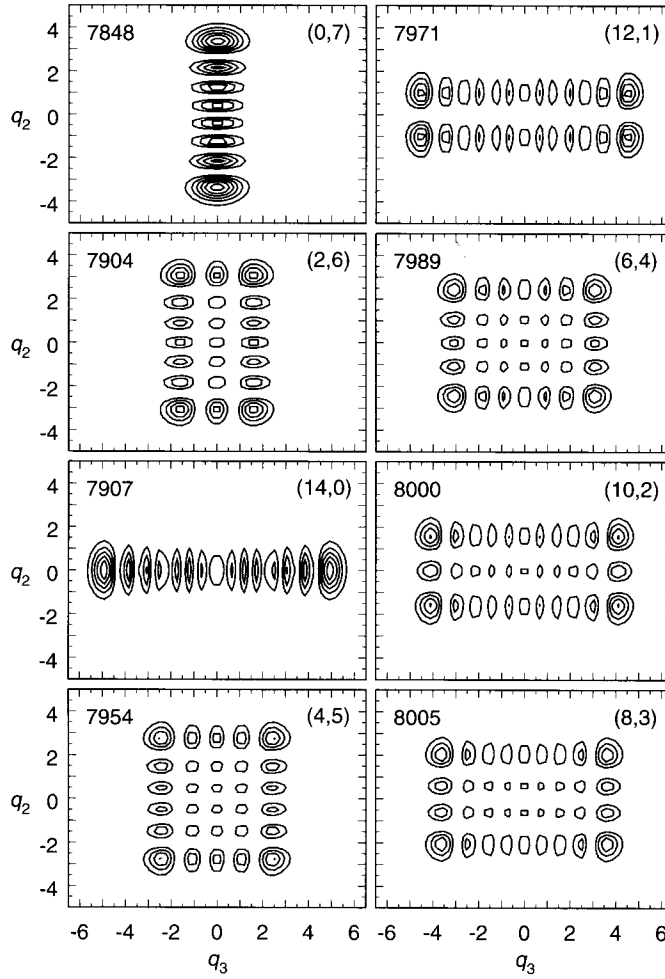

Figure 10. Density probability in the (q_3, q_2) plane for the eight states of "uncoupled" HOBr belonging to polyad $[v_u, P] = [0, 14]$. The Hamiltonian is the Dunham expansion of Eq. (24) with parameters from Table I of Ref. 41. q_3 (OBr stretch) ranges from to -6.5 to 6.5, and q_2 (bend) ranges from -5.0 to 5.0. The energy (in cm^{-1}) above the quantum mechanical ground state, as well as the good quantum numbers $(v_s, v_f) = (v_3, v_2)$, are indicated for each state.

Stated in other words, the polyad folds. The wavefunctions for the eight states belonging to polyad $[v_u, P] = [0, 14]$ of uncoupled HOBr ($H = H_D$) are plotted in Fig. 10 as an example. It is seen that the energy of the states is an increasing function of v_s from $v_s = 0$ to $v_s = 8$, but a decreasing one from $v_s = 8$ to $v_s = 14$. As a result, the polyad appears rather scrambled.

Numerically, this is most easily analyzed by rewriting the Dunham expansion of Eq. (24) in terms of coordinates, which are adapted to the polyad structure of the spectrum. One defines new sets (J_u, ψ_u), (J_P, ψ_P), and (J_0, ψ_0) of conjugate action-angle-like coordinates, according to

$$\begin{aligned}(J_u, \psi_u) &= (I_u, \varphi_u) \\ (J_P, \psi_P) &= (2I_f + I_s, \varphi_s) \\ (J_0, \psi_0) &= (2I_f, \varphi_s - \varphi_f/2)\end{aligned} \tag{29}$$

which are connected to the (I_i, φ_i) $(i = u,f,s)$ ones by a linear canonical transformation. In terms of these new variables, the Hamiltonian of Eqs. (24) and (27) is rewritten in the form

$$\begin{aligned}H_D &= \sum_{i=u,P,0} \Omega_i J_i + \sum_{i,k} X_{ik} J_i J_k + \sum_{i,k,m} Y_{ikm} J_i J_k J_m + \cdots \\ H_F &= \cos(2\psi_0)(I - J_0)\sqrt{J_0}(K + \sum_{i=u,P,0} K_i I_i + \cdots)\end{aligned} \tag{30}$$

with trivial linear relationships between the spectroscopic coefficients of Eqs. (24) and (27) and those of Eq. (30). According to Eq. (25), the quantized values of J_u and J_P associated with the quantum mechanical polyad $[v_u, P]$ are

$$\begin{aligned}J_u &= v_u + \frac{d_u}{2} \\ J_P &= P + d_f + \frac{d_s}{2}\end{aligned} \tag{31}$$

Clearly, polyad $[v_u, P]$ of the uncoupled system $H = H_D$ is folded if equation

$$\frac{\partial H_D}{\partial J_0} = 0 \tag{32}$$

has a real solution $J_0 = J_F$, such that $0 \leq J_0 \leq J_P$ (J_F is a function of J_u and J_P). The result is displayed in Fig. 11 (top) for the states of HOBr with no excitation in the OH stretch ($v_u = 0$). This figure shows the energy of (i) the pure bending trajectory [b], that is, $H_D(J_0 = J_P)$, (ii) the pure stretching trajectory [s], that is, $H_D(J_0 = 0)$, and (iii) the folding point [F], that is, $H_D(J_0 = J_F)$, as a function of P (more precisely, as a function of J_P, but the abscissa scale is converted to artificially continuous values of P according to Eq. (31)). The energies are plotted relative to the energy of [b], because they are all nearly degenerate (because of the resonance condition) and essentially linear functions of P. It is

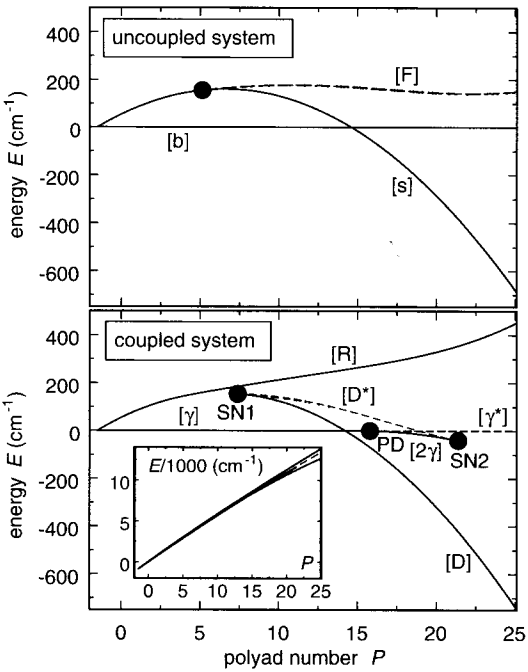

Figure 11. (**Top**) Plot, as a function of the polyad number P, of the energies of the pure bending trajectory [b], the pure stretching trajectory [s], and the folding point [F] for the states of "uncoupled" HOBr with no excitation in the OH stretch ($v_u = v_l = 0$). The Hamiltonian is the Dunham expansion of Eq. (24) with parameters from Table I of Ref. 41. All energies are plotted relative to the energy of the bending trajectory [b]. (**Bottom**) Plot, as a function of the polyad number P, of the energies of the periodic orbits for the states of HOBr with no excitation in the OH stretch ($v_u = v_l = 0$). The Hamiltonian is the Fermi resonance model of Eqs. (24) and (27), with parameters from Table I of Ref. 41. The small insert depicts the energies of the PDs relative to the energy of the quantum mechanical ground state. In the main figure, the energies are plotted relative to the energy of the pure bending periodic orbit [γ]. The heavy dots marked SN1, SN2, and PD indicate the two saddle-node and the period-doubling bifurcations, respectively. Stable periodic orbits are indicated by solid lines, while unstable periodic orbits are represented by dashed curves.

seen that polyads are folded above $P \approx 5$ and that the energy of the pure stretching trajectory [s] becomes *smaller* than the energy of the pure bending trajectory [b] at $P \approx 15$. The energies of quantum states always occur between the energies of the two outermost lines, that is, [b] and [s] up to $P = 5$, [b] and [F] from $P = 5$ to $P = 15$, and [s] and [F] above $P = 15$. Therefore, pure stretching states are located at the top of the polyads up to $P = 5$; they then migrate from the top to the bottom of the polyads between $P = 5$ and $P = 15$, and they finally reach the bottom of the polyads above $P = 15$. Conversely, pure bending states

are located at the bottom of the polyads up to $P = 15$ and then migrate inside the polyad. It is also emphasized, as can be checked in Fig. 10, that the states located at the top of the polyads above $P = 5$ are not associated with any particular motion, but are instead just combination states with $P - J_F + 1$ (or the integer closest to this value) nodes along the slow reactive coordinate and $(J_F - 1)/2$ nodes along the fast one. Similar features are observed for HOCl and HCP (in the later case, the CP stretch plays the role of the HOBr bend, and the HCP bend plays that of the OBr stretch).

Let us now consider the dynamics of the coupled system with Hamiltonian $H = H_D + H_F$. J_u and J_P remain good quantum numbers for this Hamiltonian and are quantized according to Eq. (31). It is known that the dynamics of the coupled system is governed by the shape of its stable periodic orbits (POs) in the subspace (p_s, q_s, p_f, q_f) of the normal coordinates involved in the Fermi resonance. The reason for this is that these POs act as the "backbones" (or nodal lines) of the quantum mechanical wavefunctions. Moreover, it is not necessary to consider the POs in the full six-dimensional space as long as the third mode u remains decoupled from s and f. The four-dimensional POs are most easily obtained in terms of the conjugate coordinates of Eq. (29). Indeed, they consist of the line $J_0 = J_P$, plus the fixed points in the (J_0, ψ_0) space. These fixed points satisfy

$$\begin{aligned} \frac{dJ_0}{dt} &= -\frac{\partial H}{\partial \psi_0} = 0 \\ \frac{d\psi_0}{dt} &= \frac{\partial H}{\partial J_0} = \frac{\partial H_D}{\partial J_0} + \frac{\partial H_F}{\partial J_0} = 0 \end{aligned} \tag{33}$$

Note that the first equation has trivial solutions $\psi_0 = 0$ and $\psi_0 = \pi/2$ (sometimes it also has less trivial solutions). Moreover, the derivative of H_F, in the second equation, is always much smaller than the derivative of H_D, except in the neighborhood of $J_0 = 0$, where $\partial H_F/\partial J_0$ goes to infinity, and in the neighbourhood of $J_0 = J_F$ (if the polyad folds), where $\partial H_D/\partial J_0$ goes to zero. Consequently, the coupled system has at least one fixed point with $J_0 \approx 0$ and another one with $J_0 \approx J_F$. Since, as stated above, the $J_0 = J_P$ line also corresponds to a PO in the (p_s, q_s, p_f, q_f) subspace, one can conclude that the coupled system $H = H_D + H_F$ necessarily has periodic orbits, which remain energetically close to the bend [b] and the stretch [s] trajectories, as well as the folding line [F], of the uncoupled system, for all values of P (the coupled system can have additional principal families of POs, see below). One therefore expects the continuation/bifurcation (C/B) diagram [46–48] of the coupled system—that is, the plot of the energies of the POs as a function of the polyad number P, not to be too different from the plot of the energies of [s], [b], and [F] for the uncoupled system. This point can be checked in the case of HOBr by comparing the top and

bottom plots of Fig. 11. At first glance, they are indeed rather similar. There are, however, important discrepancies that will now be discussed.

At low P values ($P \leq 7.4$), the coupled system $H = H_D + H_F$ has two stable POs, called [γ] and [R], which coincide, respectively, with the bend [b] and stretch [s] trajectories of the uncoupled system $H = H_D$. Since both [b] and [γ] satisfy $J_0 = J_P$, their energies coincide through the whole range of P values. In contrast, starting with the P value where the polyad first folds (i.e., $P = 5$), the [R] PO deviates from [s] and follows instead the folding line [F]. In agreement with the conclusions of the preceding paragraph, a stable PO, which remains close to the [s] line, that is which is essentially pure OBr stretch in the case of HOBr, however appears at $P = 7.4$. This PO, which is called [D] in the case of HOBr and HOCl, is born at a saddle-node bifurcation, which is indicated in Fig. 11 (bottom) as a black dot labeled SN1. Saddle-node bifurcations are singularities of the phase space, where a stable and an unstable PO are created simultaneously [45,49–51] (the unstable PO [D*] is indicated with a dashed line in Fig. 11). From the preceding discussion it should be clear that the saddle-node bifurcation SN1 represents the *nonlinear response of the coupled system to the folding of the polyads of the uncoupled system*. Stated in other words, it is the consequence of the coexistence of the Fermi resonance and the strong anharmonicity along the reaction pathway.

Saddle-node bifurcations taking place for the reasons just described have been observed for HOBr [41], HOCl [36,38,39], and HCP [34–36]. For HOBr and HOCl, the stable PO born at the saddle-node bifurcations is called [D] for "dissociation," because this PO stretches along the dissociation pathway and scars OBr- or OCl-stretch quantum mechanical wavefunctions (see Fig. 11e of Ref. 38, Figs. 3b and 3g of Ref. 41, or Section III.B). In the case of HCP, the stable PO born at the bifurcation is better called [I], for "isomerization," because this PO stretches along the isomerization pathway and scars bending quantum mechanical wavefunctions (see Figs. 6b and 6d of Ref. 35 or Figs. 7b and 7d of Ref. 36).

Despite the general resemblance of the energy curves in Fig. 11, the Fermi resonance has a dramatic effect on the wavefunctions, as can be checked by comparing Fig. 10 and Fig. 12, which show the wavefunctions of the eight states of polyad $[v_u, P] = [0, 14]$ for "uncoupled" ($H = H_D$) and "coupled" ($H = H_D + H_F$) HOBr, respectively. The principal reason for this striking difference is that, in addition to the OH stretch, the uncoupled system has only two degrees of freedom (the bend [b] and the OBr stretch [s]), while the coupled system has three possible types of motion above the saddle-node bifurcation: the bend [γ], an almost pure OBr stretching motion along the [D] PO, and a resonant-type motion along the [R] PO (the pronounced horseshoe shape of this later PO reflects a strong energy transfer between the OBr stretch and the bend). As a consequence, the polyads of the coupled system can no longer be described,

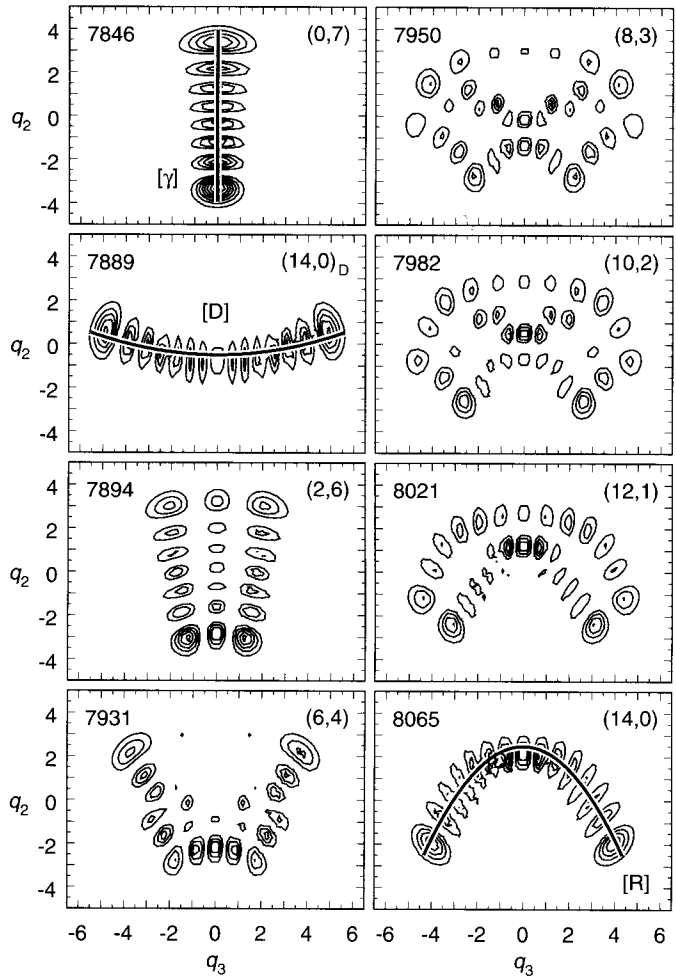

Figure 12. Density probability in the (q_3, q_2) plane for the eight states of "coupled" HOBr belonging to polyad $[v_u, P] = [0, 14]$. The Hamiltonian is the Fermi resonance Hamiltonian of Eqs. (24) and (26) with parameters from Table I of Ref. 41. q_3 (OBr stretch) ranges from to -6.5 to 6.5 and q_2 (bend) from -5.0 to 5.0. The energy (in cm^{-1}) above the quantum mechanical ground state, as well as approximate quantum numbers $(v_s, v_f) = (v_3, v_2)$, are indicated for each state. The three periodic orbits for this polyad, [R], [D], and [γ], are plotted on top of some of the density probabilities.

above $P = 5$, as the folding of regular sequences of states that evolve from a pure bending state (along [b]) to a pure OBr stretching state (along [s]). They are instead better described as sequences of states, which evolve from pure bending states (scared by the [γ] PO) to *resonant-type states* (scared by the [R] PO) and are perturbed, above the saddle-node bifurcation, by the birth and proliferation of OBr-stretching states (scared by the [D] PO).

The most detailed understanding of the evolution of the polyads of the coupled system is obtained by plotting the third action integral of the system as a function of energy E for given values of J_u and J_P. This action integral is expressed as

$$\Im = \Im(E, J_u, J_P) = \frac{1}{2\pi} \int_{\psi_0 \in [0,\pi]} J_0 \mathrm{d}\psi_0 \tag{34}$$

while the corresponding EBK quantization rule reads

$$\Im = n + \tfrac{1}{2} \tag{35}$$

where n is an integer, either positive or negative. Figure 13 provides examples of such plots for polyads $[v_u, P] = [0, 7]$, [0, 14] and [0, 30] of HOBr. The plot for polyad $[v_u, P] = [0, 7]$, which is located below the bifurcation, contains only one branch, which extends from the energy of the [γ] PO to the energy of the [R] PO and is denoted by (a). According to Eq. (35), the semiclassical energies are the values of E at which $\Im$ is half-integer. These values are indicated with filled circles in Fig. 13. It is emphasized that the quantum and semiclassical energies are in very good agreement, with the difference between the two sets of values never exceeding a few cm^{-1}. Branch (a) contains members of the normal progression of states, which evolve from a state aligned along [γ] to a state aligned along [R]. At the SN1 bifurcation, the branch (a) of the action integral splits into two branches (a) and (b). These two branches again support quantum states belonging to the normal progression. However, one state of this progression disappears each time the energy gap between (a) and (b) becomes sufficiently wide to encompass an additional half-integer value of $\Im$. For example, it can be checked in Fig. 12 that the third state of the normal progression (i.e., the state with four nodes along the [R] PO) is missing from the normal progression, because the half-integer value $\Im = -11/2$ lies in the gap between (a) and (b) (see Fig. 13). Still, the number of states in polyad P remains equal to $\mathrm{int}(P/2) + 1$, because each state, which disappears from the normal progression, is replaced by a member of the new progression of "dissociation" states, which is supported by branch (c). This third branch also appears at the saddle-node bifurcation SN1 and extends between the energies of the stable [D]

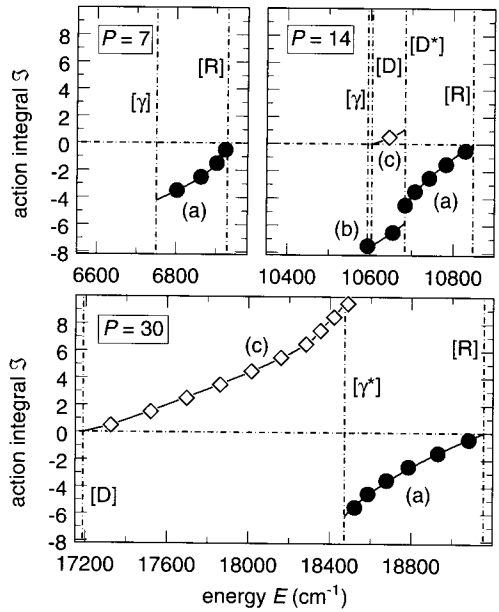

Figure 13. Plot of the action integral $\Im$ as a function of the absolute energy E for polyads $[v_u, P] = [0, 7]$, $[0, 14]$, and $[0, 30]$ of HOBr. The Hamiltonian is the Fermi resonance Hamiltonian of Eqs. (24) and (27) with parameters from Table I of Ref. 41. The vertical lines indicate the energies of the various periodic orbits. The quantum mechanical states belonging to the normal and the "new" progression are indicated by filled circles and open diamonds, respectively. Note that the horizontal energy scale for polyads $P = 7$ and $P = 14$ is expanded twice compared to $P = 30$.

and unstable [D*] POs born at the bifurcation (see $P = 14$ in Fig. 13). One additional dissociation state appears in the quantum spectrum each time branch (c) widens sufficiently to encompass an additional half-integer value of $\Im$. For example, it can be checked in Figs. 12 and 13 that the dissociation state of polyad $[v_u, P] = [0, 14]$ (i.e., the second lowest state) corresponds to $\Im = 1/2$ on branch (c). It should be realized that the number of states in polyad P remains equal to $\text{int}(P/2) + 1$, because branches (b) and (c) are parallel in the energy interval where they overlap (the classical frequency is the same for the two branches).

B. Bifurcations at Higher Energies

The saddle-node bifurcations discussed in Section III.A play a crucial role in the dynamics of the molecules investigated, because the stable PO born at the bifurcation follows the reaction pathway over a large energy range. Consequently, the quantum states that are scarred by this PO stretch further and further along the reaction pathway and can be considered as the precursors of the

isomerization and dissociation reactions. Nonetheless, increasing the energy deposited in the vibrational degrees of freedom of these molecules results in additional bifurcations, which are discussed in this section.

Part of these additional bifurcations are reproduced by the Fermi resonance Hamiltonian. For example, the C/B diagram of HOBr in Fig. 11 displays, in addition to SN1, two further bifurcations, PD and SN2, which take place at $P = 15.8$ and $P = 21.4$, respectively. PD is a period-doubling bifurcation, where the bending-type PO [γ], defined by $J_0 = J_P$, becomes unstable, while the double-period daughter PO remains stable. This stable PO with double period, called [2γ], is found in a rather restricted interval of P values, since it disappears at the second saddle-node bifurcation SN2. In contrast with SN1, where the stable [D] and the unstable [D*] POs were *born* simultaneously, SN2 corresponds to a discontinuity of the classical phase space, where the stable [2γ] and the unstable [D*] POs are *destroyed* simultaneously. At SN2, branch (b) disappears from the plot of the action integral $\Im$ as a function of energy E. Therefore, for polyads $[v_u = 0, P]$ where $P \geq 22$, the accessible classical phase space extends between the two remaining stable POs—that is, [D] and [R]—with the unstable PO [$\gamma*$] playing the role of a separatrix between the two kinds of motion (see Fig. 13, $P = 30$). Quantum mechanically, all the members of the new progression are located below [$\gamma*$], on the (c) branch, while all the remaining members of the normal progression are located above [$\gamma*$], on the (a) branch (see Fig. 13, $P = 30$). The question regarding why polyads $[v_u, P]$ with $22 \leq P \leq 35$ look simpler than polyads at lower energies is explained by the following facts: (i) There remain only two stable POs, and therefore two possible backbones for quantum mechanical wavefunctions, and (ii) members of the normal and new progression can no longer be interwoven. This point can be checked in Fig. 5 of Ref. 41, which shows the wavefunctions for the 16 states belonging to polyad $[v_u, P] = [0, 30]$ of HOBr.

To conclude this analysis based on the Fermi resonance Hamiltonian, let us mention that HOCl, behaves very much like HOBr. Indeed, Fig. 10b of Ref. 36 shows that for this molecule the saddle-node bifurcation SN1 takes place at $P = 21.8$, (for $v_u = 0$), the period-doubling bifurcation PD occurs at $P = 24.6$, and the second saddle-node bifurcation SN2 takes place at around $P = 38$, very close to the dissociation threshold. In contrast, the dynamics of HCP is somewhat simpler, in the sense that the first saddle-node bifurcation SN1 is indeed observed at $P = 14.3$, but PD and SN2 do not take place (see Fig. 13 of Ref. 35 or Fig. 10a of Ref. 36).

Most of the bifurcations, which take place in the high-energy regime, are however not reproduced by the Fermi resonance Hamiltonian, essentially because they result from the superposition of the 1:2 Fermi-resonance and higher-order ones. In order to gain information on the dynamics close to the reaction threshold, one therefore has to analyze the dynamics on the PES by

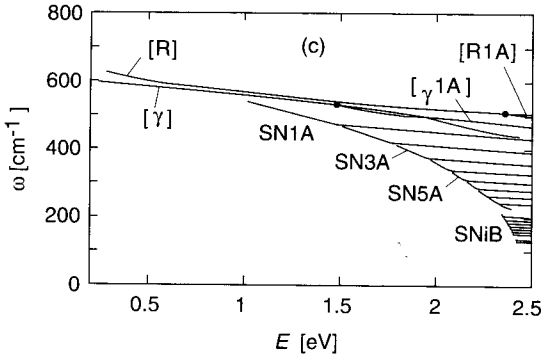

Figure 14. Plot, as a function of the absolute energy E, of the frequencies of the classical periodic orbits belonging to various families. The frequencies of the [γ]-type POs are divided by two, whereas the frequencies of the [R1A] family are multiplied by two. The energy scale is shifted to higher energies by 0.23 eV—that is, the zero-point energy of the OH stretch mode. See the text for more details.

classical mechanics. These studies have been performed for the three molecules already discussed—that is, HOBr [41], HOCl [38], and HCP [35,36]. It turns out that cascades of saddle-node bifurcations seem to be the rule when approaching the reaction threshold. One can distinguish between two different types of cascades, according to the types of motion involved in the bifurcations.

The first type of cascade has been observed for all three of the molecules, HOBr, HOCl, and HCP. Figure 14 shows, for example, the classical C/B diagram obtained for HOBr (see Fig. 5d of Ref. 38 for the classical C/B diagram of HOCl and Fig. 9b of Ref. 35 or Fig. 8b of Ref. 36 for the classical C/B diagram of HCP). Since there is no conserved quantity, except the energy E, classical C/B diagrams necessarily represent the evolution with respect to E of a given property of the POs, like, for example, their frequencies, as in Fig. 14. In this diagram it is seen that the SN1 bifurcation and the smooth [D] curve of the Fermi resonance model in Fig. 11 are replaced by a series of SNiA bifurcations and corresponding [SNiA] curves ($i = 1, 2, 3, \ldots$), which all exhibit the same pattern, namely, a short segment with a relatively large anharmonicity and a second segment for which the slope is very small. The nearly flat segment of each curve is probably due to a resonance between motion along the successive [SNiA] POs and the OH stretch [41]. Roughly speaking, the [D] line of the Fermi resonance model in Fig. 11 is just the smooth interpolation between successive segments with large anharmonicities. Since the POs that scar dissociating quantum states (i.e., states stretching along the dissociation pathway) all belong to the more anharmonic segments of the [SNiA] curves, the more harmonic segments of the C/B diagram in Fig. 14 are not essential to

understand the features of the quantum mechanical spectrum: The [D] line joining the more anharmonic segments contains all the important information.

The successive [SN*i*A] POs follow closely the dissociation pathway up to [SN7A], while they acquire a pronounced S-type shape and ultimately avoid the dissociation pathway for $i \geq 8$, as is illustrated in Figs. 15b and 15f. This happens in the same energy range where a second cascade of saddle-node bifurcations SN*i*B and related stable POs [SN*i*B] are first observed (see Fig. 14). This is not by chance. What one observes here is indeed just the repetition—with a different ratio of the classical frequencies—of the scheme, which gives rise to the SN*i*A family of saddle-node bifurcations at lower energies. More precisely, in Section III.A it was seen that the 1:2 Fermi resonance between motions along [R] (OBr stretch) and [γ] (bend) is responsible for (i) the pronounced U shape that [R] acquires with increasing energies (see Fig. 15c), and (ii) the occurrence of the saddle-node bifurcations SN1 (or SN*i*A), where a new motion along [D] (or [SN*i*A]) is born, which follows the reaction pathway (see Fig. 15b). Because of the large anharmonicity along the reaction pathway, the frequency of the motion along [SN*i*A] however steadily decreases with increasing energies, so that at a certain point a 1:3 resonance with the motion along the bending type PO [γ] is established. As happened for the 1:2 resonance between [R] and [γ], the 1:3 resonance between [SN*i*A] and [γ] is responsible for (i) the pronounced S-shape that [SN*i*A] aquires above SN7A (see Fig. 15f) and (ii) the occurrence of a second family of saddle-node bifurcations, SN*i*B, where a new motion along the [SN*i*B] POs is born, which follows the reaction pathway (see Fig. 15g). Note that because of resonances with the OH-stretch degree of freedom, each [SN*i*B] curve has the same pattern as the [SN*i*A] ones, namely, a short segment with a relatively large anharmonicity and a second segment for which the slope is very small.

From the classical point of view, the high-energy bifurcation pattern of HOBr thus consists of two nested cascades of saddle-node bifurcations. The principal cascade, R $\rightarrow$ SN*i*A $\rightarrow$ SN*i*B $\rightarrow$ ..., results from the successive 1:2, 1:3, and so on, resonances between the OBr stretch and the bend. Each member of the principal family, in turn, consists of a cascade of bifurcations, SN1A $\rightarrow$ SN2A $\rightarrow$ SN3A $\rightarrow$ ... and SN1B $\rightarrow$ SN2B $\rightarrow$ SN3B $\rightarrow$ ..., because of resonances between the OBr stretch and the OH stretch. From the quantum mechanical point of view, one observes, above the onset of the 1:3 resonance, states that are scared by the three possible "stretching"-type POs, that is, [R] (U-shaped wavefunctions), [SN*i*A] (S-shaped wavefunctions), and [SN*i*B] (wavefunctions stretching along the dissociation pathway).

Two points are worth noting before concluding. First, the ab initio PES for HOBr [40,41] is the only realistic molecular model, for which such a subtle pattern of bifurcations has been detected so far: For HOCl [38] and HCP [35], the SN*i*B family of saddle-node bifurcations could not be found. Moreover, both

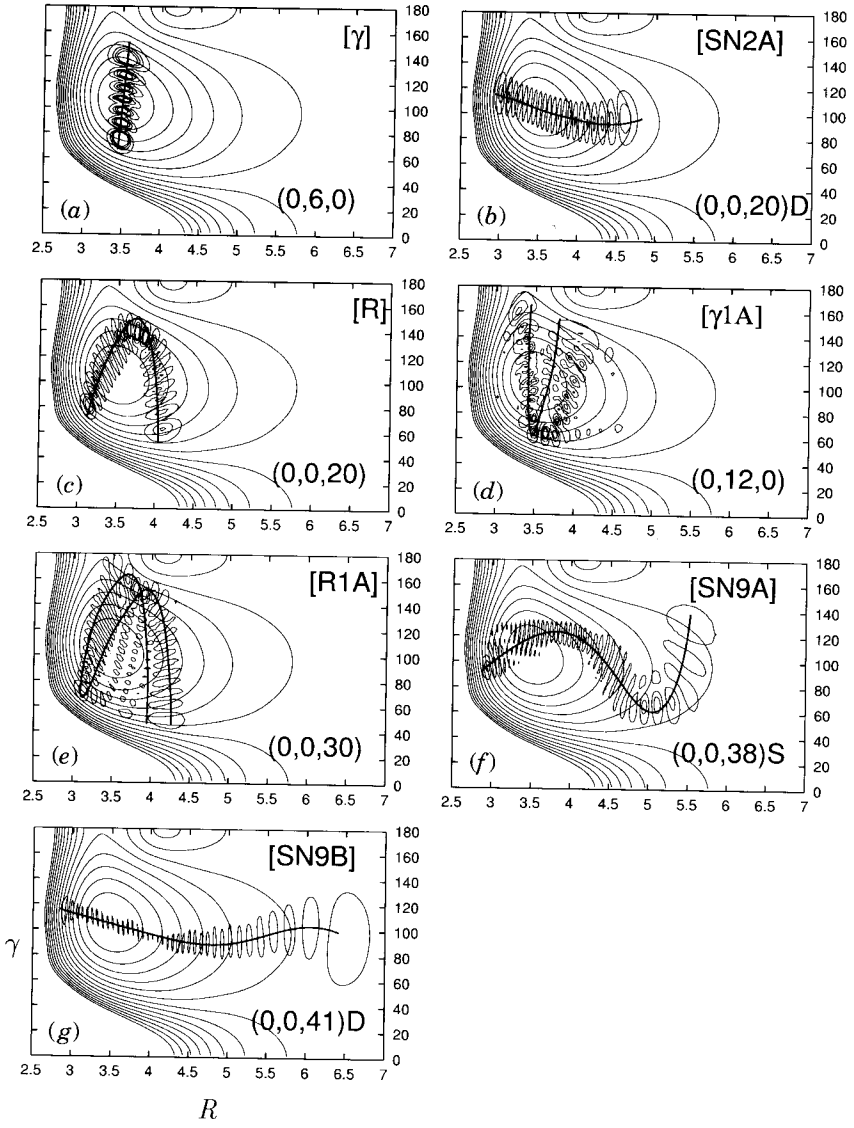

Figure 15. Contour plots of wavefunctions for different types of quantum mechanical states as functions of R and γ. The OH-stretch coordinate r is integrated over. The solid lines represent corresponding classical periodic orbits calculated at comparable energies.

HOCl and HOBr display a couple of additional bifurcations, which were not discussed here because they are not directly related to the dissociation reaction. The interested reader is referred to Refs. 38 and 41 for more details.

IV. SUMMARY

The character of vibrational states of a polyatomic molecule is expected to drastically change with increasing internal energy. This has been demonstrated in this review for several triatomic molecules: HCN, HCP, HOCl, and HOBr. For the first two examples, increasing the energy gradually "drives" the molecule toward the isomerization barrier, while for the other two examples it pushes the molecule toward the dissociation channel. In both cases, the types of vibrational motion are very different from the motion at low energies. Exact quantum mechanical, classical, and semiclassical methods have been utilized to discuss this development from low to high energies.

For HCN, a molecule with no resonance between the three fundamental frequencies, we have demonstrated that a sequence of canonical transformations leads to a nearly separable Hamiltonian, the diagonalization of which quantitatively predicts the eigenenergies. Moreover, this approximate Hamiltonian is well suited to describe the localized as well as part of the delocalized states of the system and leads to a consistent assignment of most of the states. Nevertheless, the remaining couplings, which are ignored in the transformed Hamiltonian, lead to interesting delocalized states, which require a full quantum mechanical description. These states, which have different stretching excitations in the HCN and the CNH wells, have been termed "nonadiabatically delocalized" states, because they are due to couplings between states belonging to different adiabatic channels.

The other three molecules are different in that they show already at low energies a 1:2 Fermi resonance between the reaction (isomerization or dissociation) coordinate and another coordinate. This resonance, together with the polyad folding due to the strong anharmonicity in the isomerization or dissociation mode, leads to saddle-node bifurcations, at which new types of states come into existence and members of progressions characteristic for the lower-energy regime disappear. The new family of states advances the molecule toward the isomerization barrier or the dissociation channel. The existence of saddle-node bifurcations usually makes the spectrum of eigenenergies and the organization in terms of polyads quite complex. However, we have also shown how a detailed analysis of the structure of the classical phase space in terms of periodic orbits and continuation/bifurcation diagrams can be used to understand the quantum mechanical spectrum. Saddle-node bifurcations seem to be characteristic features of many molecules. However, up to now an experimental example has only been observed for HCP [35].

A detailed understanding of the intramolecular motion of highly excited molecules is important for understanding the dissociation dynamics, because the sequences of bound states just below the dissociation threshold continue as resonances to energies above the threshold [52]. Whether the dynamics around the threshold is chaotic or whether the eigenstates show characteristic features will have consequences for the lifetime of the excited complex and therefore on the dissociation rate. The same is true, of course, also for the inverse process—that is, the stabilization of complexes in collisions with gas atoms.

References

1. M. Joyeux and D. Sugny, *Can. J. Phys.* **80**, 1459 (2002).
2. D. Sugny, M. Joyeux, and E. L. Sibert III, *J. Chem. Phys.* **113**, 7165 (2000).
3. D. Sugny and M. Joyeux, *J. Chem. Phys.* **112**, 31 (2000).
4. K. Efstathiou, M. Joyeux, and D.A. Sadovskii, *Phys. Rev. A*, **69**, 032504 (2004).
5. M. Joyeux, D. A. Sadovskii, and J. Tennyson, *Chem. Phys. Lett.* **382**, 439 (2003).
6. J. Robert and M. Joyeux, *J. Chem. Phys.* **119**, 8761 (2003).
7. T. van Mourik, G. J. Harris, O. L. Polyansky, J. Tennyson, A. G. Csaszar, and P. J. Knowles, *J. Chem. Phys.* **115**, 3706 (2001).
8. G. J. Harris, O. L. Polyansky, and J. Tennyson, *Spectrochim. Acta A* **58**, 673 (2002).
9. E. B. Wilson, J. C. Decius, and P. C. Cross, *Molecular Vibrations*, Dover, New York, 1955, Chapter 4.
10. J. H. Van Vleck, *Phys. Rev.* **33**, 467 (1929).
11. O. M. Jordahl, *Phys. Rev.* **45**, 87 (1934).
12. E. C. Kemble, *The Molecular Principles of Quantum Mechanics*, McGraw-Hill, New York, 1937, Section 48c.
13. E. L. Sibert III, *J. Chem. Phys.* **88**, 4378 (1988).
14. D. Lessen, J. S. Baskin, C. M. Jones, T. He, and E. Carrasquillo-Molina, *J. Chem. Phys. A* **107**, 5697 (2003).
15. I. Shavitt and L. T. Redmon, *J. Chem. Phys.* **73**, 5711 (1980).
16. A. J Dragt and J. M. Finn, *J. Math. Phys.* **17**, 2215 (1976).
17. A. J Dragt and J. M. Finn, *J. Math. Phys.* **20**, 2649 (1979).
18. A. J Dragt and E. Forest, *J. Math. Phys.* **24**, 2734 (1983).
19. G. D. Birkhoff, *Dynamical Systems*, Vol. 9, AMS colloquium, AMS, New York, 1966.
20. F. G. Gustavson, *Astron. J.* **71**, 670 (1966).
21. R. T. Swimm and J. B. Delos, *J. Chem. Phys.* **71**, 1706 (1979).
22. A. M. Smith, S. L. Coy, W. Klemperer, and K. K. Lehmann, *J. Mol. Spectrosc.* **134**, 134 (1989).
23. X. Yang, C. A. Rogaski, and A. M. Wodtke, *J. Opt. Soc. Am. B* **7**, 1835 (1990).
24. D. M. Jonas, X.Yang, and A. M. Wodtke, *J. Chem. Phys.* **97**, 2284 (1992).
25. S. C. Farantos, J. M. Gomez Llorente, O. Hahn, and H. S. Taylor, *J. Chem. Phys.* **93**, 76 (1990).
26. D. Romanini, and K. K. Lehmann, *J. Chem. Phys.* **102**, 633 (1995).
27. A. Maki, W. Quapp, S. Klee, G. C. Mellau, and S. Albert, *J. Mol. Spectrosc.* **180**, 323 (1996).
28. F. J. Northrup, G. A. Bethardy, and R. G. Macdonald, *J. Mol. Spectrosc.* **186**, 349 (1997).

29. J. M. Bowman, B. Gazdy, J. A. Bentley, T. K. Lee, and C. E. Dateo, *J. Chem. Phys.* **99**, 308 (1993).
30. Z. Bacic, R. M. Whitnell, D. Brown, and J. C. Light, *Comput. Phys. Comm.* **51**, 35 (1988).
31. A. J. Dobbyn, M. Stumpf, H.-M. Keller, and R. Schinke, *J. Chem. Phys.* **103**, 9947 (1995).
32. D. J. Nesbitt and R. W. Field, *J. Phys. Chem.* **100**, 12735 (1996).
33. C. Beck, R. Schinke, and J. Koput, *J. Chem. Phys.* **112**, 8446 (2000).
34. M. Joyeux, D. Sugny, V. Tyng, M. E. Kellman, H. Ishikawa, R. W. Field, C. Beck, and R. Schinke, *J. Chem. Phys.* **112**, 4162 (2000).
35. H. Ishikawa, R. W. Field, S. C. Farantos, M. Joyeux, J. Koput, C. Beck, and R. Schinke, *Annu. Rev. Phys. Chem.* **50**, 443 (1999).
36. M. Joyeux, S. C. Farantos, and R. Schinke, *J. Phys. Chem. A* **106**, 5407 (2002).
37. S. Skokov, K. A. Peterson, and J. M. Bowman, *J. Chem. Phys.* **109**, 2662 (1998).
38. J. Weiss, J. Hauschildt, S. Yu. Grebenshchikov, R. Düren, R. Schinke, J. Koput, S. Stamatiadis, and S. C. Farantos, *J. Chem. Phys.* **112**, 77 (2000).
39. R. Jost, M. Joyeux, S. Skokov, and J. M. Bowman, *J. Chem. Phys.* **111**, 6807 (1999).
40. K. A. Peterson, *J. Chem. Phys.* **113**, 4598 (2000).
41. T. Azzam, R. Schinke, S. C. Farantos, M. Joyeux, and K. A. Peterson, *J. Chem. Phys.* **118**, 9643 (2003).
42. A. Einstein, *Verh. Dtsch. Phys. Ges.* **19**, 82 (1917).
43. L. Brillouin, *J. Phys.* **7**, 353 (1926).
44. J. Keller, *Ann. Phys.* **4**, 180 (1958).
45. M. Tabor, *Chaos and Integrability in Nonlinear Dynamics*, John Wiley & Sons, New York, 1989.
46. S. Wiggins, *Global Bifurcations and Chaos*, Springer, Berlin, 1988.
47. S. Wiggins, *Introduction to applied nonlinear dynamical systems and chaos*, Springer, New York, 1990.
48. S. C. Farantos, *Int. Rev. Phys. Chem.* **15**, 345 (1996).
49. P. Berge, Y. Pomeau, and C. Vidal, *Order Within Chaos*, John Wiley & Sons, New York, 1984.
50. M. C. Gutzwiller, *Chaos in Classical and Quantum Mechanics*, Springer, New York, 1990.
51. J. Guckenheimer and P. Holmes, *Nonlinear Oscillations, Dynamical Systems, and Bifurcations of Vector Fields*, Springer, Berlin, 1983.
52. S. Yu. Grebenshchikov, R. Schinke, and W. L. Hase, *State-Specific Dynamics of Unimolecular Dissociation*, in N. J. B. Green, ed., *Comprehensive Chemical Kinetics*, Vol. 39, Part I, Elsevier, Amsterdam, 2003.